

Electron density distribution of $LiMn_2O_4$ cathode investigated by synchrotron powder x-ray diffraction

Tongtong Shang(尚彤彤), Dongdong Xiao(肖东东), Qinghua Zhang(张庆华), Xuefeng Wang(王雪锋), Dong Su(苏东), and Lin Gu(谷林)

Citation: Chin. Phys. B, 2021, 30 (**7**): 078202. DOI: 10.1088/1674-1056/abf347
Journal homepage: http://cpb.iphy.ac.cn; http://iopscience.iop.org/cpb

What follows is a list of articles you may be interested in

Silicon micropillar electrodes of lithiumion batteries used for characterizing electrolyte additives

Fangrong Hu(胡放荣), Mingyang Zhang(张铭扬), Wenbin Qi(起文斌), Jieyun Zheng(郑杰允), Yue Sun(孙悦), Jianyu Kang(康剑宇), Hailong Yu(俞海龙), Qiyu Wang(王其钰), Shijuan Chen(陈世娟), Xinhua Sun(孙新华), Baogang Quan(全保刚), Junjie Li(李俊杰), Changzhi Gu(顾长志), and Hong Li(李泓)
Chin. Phys. B, 2021, 30 (**6**): 068202. DOI: 10.1088/1674-1056/abf558

Suppressing transition metal dissolution and deposition in lithium-ion batteries using oxide solid electrolyte coated polymer separator

Zhao Yan(闫昭), Hongyi Pan(潘弘毅), Junyang Wang(汪君洋), Rusong Chen(陈汝颂), Fei Luo(罗飞), Xiqian Yu(禹习谦), Hong Li(李泓)
Chin. Phys. B, 2020, 29 (**8**): 088201. DOI: 10.1088/1674-1056/ab9610

Improved electrochemical performance of $Li(Ni_{0.6}Co_{0.2}Mn_{0.2})O_2$ at high charging cut-off voltage with $Li_{1.4}Al_{0.4}Ti_{1.6}(PO_4)_3$ surface coating

Yi Wang(王怡), Bo-Nan Liu(刘柏男), Ge Zhou(周格), Kai-Hui Nie(聂凯会), Jie-Nan Zhang(张杰男), Xi-Qian Yu(禹习谦), Hong Li(李泓)
Chin. Phys. B, 2019, 28 (**6**): 068202. DOI: 10.1088/1674-1056/28/6/068202

Improved electrochemical performances of high voltage $LiCoO_2$ with tungsten doping

Jie-Nan Zhang(张杰男), Qing-Hao Li(李庆浩), Quan Li(李泉), Xi-Qian Yu(禹习谦), Hong Li(李泓)
Chin. Phys. B, 2018, 27 (**8**): 088202. DOI: 10.1088/1674-1056/27/8/088202

Redox-assisted Li^+-storage in lithium-ion batteries

Qizhao Huang(黄启昭) and Qing Wang(王庆)
Chin. Phys. B, 2016, 25 (**1**): 018213. DOI: 10.1088/1674-1056/25/1/018213

RAPID COMMUNICATION

Electron density distribution of $LiMn_2O_4$ cathode investigated by synchrotron powder x-ray diffraction*

Tongtong Shang(尚彤彤)[1,2], Dongdong Xiao(肖东东)[1,3,†], Qinghua Zhang(张庆华)[1,4,‡], Xuefeng Wang(王雪锋)[1,2], Dong Su(苏东)[1,2], and Lin Gu(谷林)[1,2,3,§]

[1] *Beijing National Laboratory for Condensed Matter Physics, Institute of Physics, Chinese Academy of Sciences, Beijing* 100190, *China*
[2] *School of Physical Sciences, University of Chinese Academy of Sciences, Beijing* 100049, *China*
[3] *Songshan Lake Materials Laboratory, Dongguan* 523808, *China*
[4] *Yangtze River Delta Physics Research Center Co. Ltd., Liyang* 213300, *China*

(Received 3 March 2021; revised manuscript received 22 March 2021; accepted manuscript online 30 March 2021)

Electron density plays an important role in determining the properties of functional materials. Revealing the electron density distribution experimentally in real space can help to tune the properties of materials. Spinel $LiMn_2O_4$ is one of the most promising cathode candidates because of its high voltage, low cost, and non-toxicity, but suffers severe capacity fading during electrochemical cycling due to the Mn dissolution. Real-space measurement of electron distribution of $LiMn_2O_4$ experimentally can provide direct evaluation on the strength of Mn–O bond and give an explanation of the structure stability. Here, through high energy synchrotron powder x-ray diffraction (SPXRD), accurate electron density distribution in spinel $LiMn_2O_4$ has been investigated based on the multipole model. The electron accumulation between Mn and O atoms in deformation density map indicates the shared interaction of Mn–O bond. The quantitative topological analysis at bond critical points shows that the Mn–O bond is relatively weak covalent interaction due to the oxygen loss. These findings suggest that oxygen stoichiometry is the key factor for preventing the Mn dissolution and capacity fading.

Keywords: lithium-ion batteries, $LiMn_2O_4$, electron density distribution

PACS: 82.47.Aa, 82.45.Fk, 71.20.–b **DOI:** 10.1088/1674-1056/abf347

1. Introduction

Lithium ion batteries (LIBs) with high energy density, low self-discharge, and long cycle life have become the most popular energy storage devices in portable electronics and electric vehicles.[1–3] Among cathode materials, spinel $LiMn_2O_4$ has the advantages of inexpensive, nontoxicity, and good safety.[4,5] However, the commercial application of this cathode is limited by the severe capacity fading during electrochemical cycling due to the Mn dissolution.[6,7] Many strategies have been proposed to improve the structure stability and cycling performance, such as doping[8–10] and design of nanostructures.[11] Real-space measurement of electron distribution of $LiMn_2O_4$ experimentally can provide direct evaluation on the strength of Mn–O bond and understand the intrinsic mechanism of capacity fading.

Considerable progress has been made on electron density measurement and related properties of materials through x-ray diffraction (XRD),[12–15] such as inter-icosahedral bonding in boron polymorphs,[16] additional charge concentration perpendicular to the bond path in Sc_3TMC_4 (TM = Fe, Co, Ni),[17] etc. Besides, the density-based quantum theory of atoms in molecules developed by Bader provides a powerful tool for interpreting the x-ray determined charge densities.[18–20] This allows for the characterization of the nature of chemical interactions between bonded atoms in molecular rather than simple connection of atoms. Kasai *et al.* found the van der Waals interactions between interlayer S–S in TiS_2 through quantitative topological analysis of measured electron density, which cannot be calculated by density functional theory (DFT).[21]

Compared with single-crystal XRD, powder diffraction has the advantages of reduced systematic errors with the negligible absorption and extinction effects, as well as the same scale factor.[13,22,23] However, some shortages to be noticed are the peaks overlapping at high scattering-angle part and the difficulty of treatment on background. Benefiting from stable third-generation synchrotron x-ray sources,[24–26] the high-quality diffraction data allow more precise determination on electron density. In this work, we investigated the electron density distribution of cathode material $LiMn_2O_4$ using high

*Project supported by Beijing Natural Science Foundation, China (Grant No. Z190010), the National Key Research and Development Program of China (Grant No. 2019YFA0308500), the Strategic Priority Research Program of Chinese Academy of Sciences (Grant No. XDB07030200), Key Research Projects of Frontier Science of Chinese Academy of Sciences (Grant No. QYZDB-SSW-JSC035), and the National Natural Science Foundation of China (Grant Nos. 51421002, 51672307, 51991344, 52025025, and 52072400).

†Corresponding author. E-mail: dongdongxiao@iphy.ac.cn
‡Corresponding author. E-mail: zqh@iphy.ac.cn
§Corresponding author. E-mail: l.gu@iphy.ac.cn

© 2021 Chinese Physical Society and IOP Publishing Ltd

energy SPXRD and multipole model. Through the topological analysis of the chemical interaction of Mn–O bond based on the measured electron density, a relatively weak covalency of Mn–O bond is characterized. Also, the relationship between the electron density and electrochemical properties is discussed.

2. Experimental details

The polycrystalline powder $LiMn_2O_4$ was brought from Alfa with metals basis of 99.5%. SEM image showed that the particle size is about 2–5 μm. The electrochemical curve of $LiMn_2O_4$ cell with Li metal as a negative electrode was operated in voltage of 3.09–4.46 V. The atomic structures of the $LiMn_2O_4$ were characterized using an ARM-200CF (JEOL, Tokyo, Japan) transmission electron microscope operated at 200 kV and equipped with double spherical aberration (Cs) correctors. High-angle angular dark-field (HAADF) and angular bright-field (ABF) images were acquired at acceptance angles of 90–370 mrad and 12–24 mrad, respectively.

Before collecting the synchrotron XRD data, the lab XRD with Cu K_α radiation was done to determine the crystallinity and structure of the sample. Polycrystalline samples of $LiMn_2O_4$ were sealed in a 0.3 mm internal diameter Lindeman glass capillary. Synchrotron powder x-ray profiles were measured at the SPring-8 BL19B2 beamline. A large Debye–Sherrer camera with an imaging plate (IP) detector was used for data collection. The data were collected at room temperature to avoid the phase transition below 280 K. The wavelength of the incident x-rays was 0.413269 Å by calibration with a National Institute of Standards and Technology (NIST) CeO_2 standard sample. Data were collected with 2θ from 2.1° to 78.165° and step width of 0.005° which guarantee the enough resolution for refinement. To subtract the contribution of glass capillary on the background intensity, diffraction data of an empty Lindeman glass capillary was also collected under the same condition.

3. Results and discussion

Figure 1 shows the atomic structure and electrochemical performance of the spinel $LiMn_2O_4$. The structure projected along [100] zone axis exbibits the typical spinel atomic arrangement as shown in Fig. 1(a), where Li ions occupy the 8*a* sites with tetrahedral coordination, Mn ions being in the 16*d* sites with octahedral coordination, and the O ions in the 32*e* sites. The [MnO_6] octahedra share faces with the [LiO_4] tetrahedra. The uniform morphology and particle size between 2–5 μm can also be visualized in Fig. 1(b). To examine the structure and crystallinity of $LiMn_2O_4$, laboratory XRD with Cu K_α has been performed as illustrated in Fig. 1(c). Through Rietveld refinement the space group is defined by *Fd-3m*. Also, the good *R* factors prove that no impurity phase exists. HAADF- and ABF-STEM images along the [110] zone axis exhibited in Figs. 1(e)–1(f) show the homogeneous atomic structure of spinel $LiMn_2O_4$.

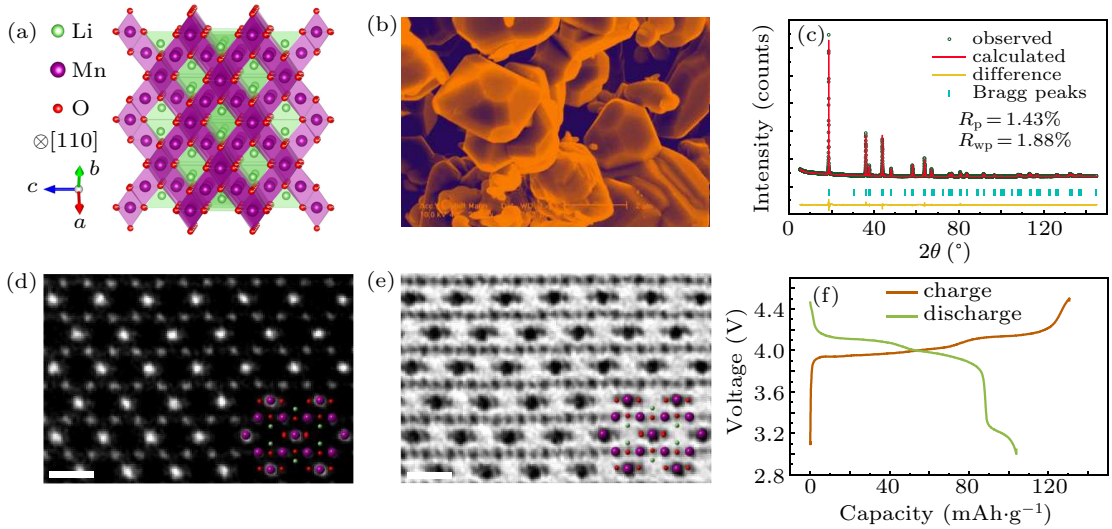


Fig. 1. Structural characterization and electrochemical performance of the spinel $LiMn_2O_4$ cathode. (a) Structure model of spinel $LiMn_2O_4$ projected along [110] zone axis. (b) Low-magnification SEM image of polycrystalline $LiMn_2O_4$ grains. (c) Refined XRD pattern acquired in lab facility. (d)–(e) HAADF and ABF images along [110] direction, where the structural models of $LiMn_2O_4$ are overlayered. Scale bar: 0.5 nm. (f) Capacity-voltage curve of $LiMn_2O_4$ cathode with Li metal as a negative electrode in the first charge/discharge cycle.

To further confirm the performance of $LiMn_2O_4$, the first electrochemical charge/discharge cycling was carried out as shown in Fig. 1(f). The severe capacity fading after initial charging is partially from the high cut-off charge voltage up to 4.46 V. The chemical composition analysis was characterized by inductively coupled plasma-mass spectrometry (ICP-MS) and the weight percent (wt%) of the three elements Li, Mn, and O can be seen in Table 1. The result shows that the content of oxygen is slightly lower than stoichiometry. This may cause the capacity fading because the oxygen deficiency can lead

to the increasing of Mn^{3+} dissolution.[27] The small oxygen deficiencies have little influence on the structure framework of pristine $LiMn_2O_4$ as shown in HAADF and ABF images. Thus, it assumes that the arrangement of oxygen deficiencies is homogeneous and disordered.

Table 1. Chemical composition obtained by inductively coupled plasma of $LiMn_2O_4$.

Element	wt%	Stoichiometric ratio
Li	3.9	1
Mn	62.8	2.034
O	33.6	3.737

Table 2. Refined results of $LiMn_2O_4$.

Parameter	Refinement results
$R(F^2)$ (%)	4.95
$wR(F^2)$ (%)	5.71
Cell parameter	8.24198(3)
z(O)	0.2656(5)
U_{11}(Li) (Å^2)	0.0182(19)
U_{1111}, U_{1112}, U_{1122},	0.00077(9) 0.00011(3) 0.00023(3) 0.00000(4)
U_{1123}(Mn) (Å^2)	0.00023(3) 0.00011(3) 0.00077(9)
U_{111}, U_{112}, U_{123}(O) (Å^2)	0.0009(8) 0.0014(3) 0.0004(7)
κ, κ' (Mn)	1.10(5) 0.93(7)
κ, κ' (O)	0.93(2) 0.78(6)
Pv (Mn)	5.68(17)
Pv (O)	6.66(8)

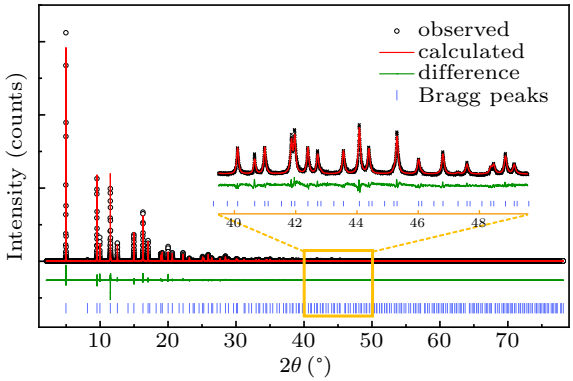


Fig. 2. Synchrotron powder XRD data and Rietveld refinement results for $LiMn_2O_4$. The inset is the magnified image from the orange box. Black cross is observed data. Red line is the corresponding calculated one. Green line is the difference between experimentally observed and calculated data. Blue vertical bar is the Bragg peak position.

The synchrotron powder x-ray diffraction was collected with $\sin\theta/\lambda_{max} = 1.52$ Å^{-1} that is enough for multipole refinement according to the condition that $\sin\theta/\lambda_{max} \geq 1.0$ Å^{-1}.[13] To reduce the systematic error caused by unapt modeling of background, a combination linear interpolation and 20 terms of Legendre polynomial expansion were used. The linear interpolation between 16 points was manually selected and adjusted to make sure that it did not inappropriately describe data features. As the diffraction data was collected at room temperature, the contribution of atomic displacement parameter (ADP) on diffraction intensity cannot be neglected. After testing different orders of ADP, the best refinement of ADPs for different atoms is anisotropic 2-order for Li, 3-order for O, and 4-order for Mn. It should be noted that two constrains for Li were imposed during multipole refinement: the valence population fixed to be 0, and the deformation valence electron was not refined. The refinement parameters exhibited in Table 2 after multipole refinement show the acceptable results according to the R factors. Figure 2 plots the multipole model and experimental data after multipole refinement. Table 2 lists some refinement parameters.[28] The refined valence populations of Mn and O are 5.68 and 6.66, respectively, in which the number of transferred electrons is lower than that of the classical valence state, indicating the covalence of Mn–O bond.

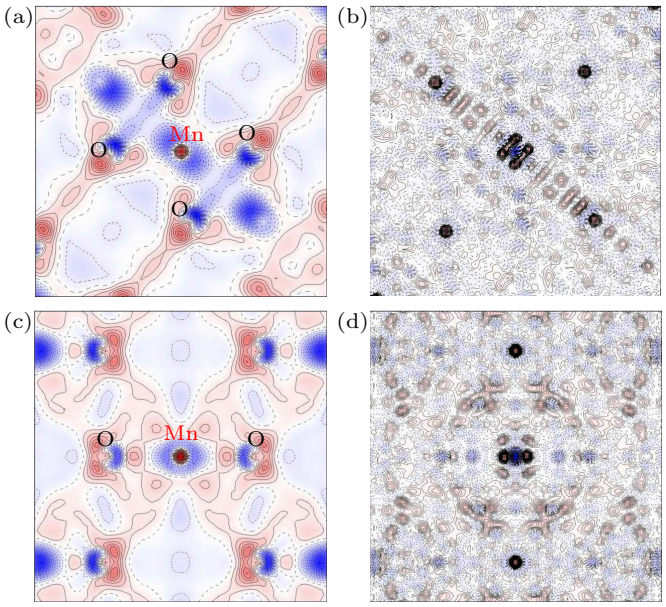


Fig. 3. Deformation charge density distribution and residual density maps of $LiMn_2O_4$. (a) and (b) are the static multipole deformation density and the corresponding residual density maps in the (010) plane. (c) and (d) are the static multipole deformation density and the corresponding residual density maps in the (110) plane. The contour interval is 0.1 e·Å^{-3}, with positive and negative contours drawn as solid red and dotted blue lines, respectively.

Figure 3 shows the static multipole deformation density and residual density of (010) and (110) planes containing Mn–O bonding of [MnO_6] octahedron. The residual density map obtained from the difference between multipole model and experiment reflects the quality of the refinement. There is accumulation of residual density at and near the nuclei, but no obvious features of valence electrons which can be seen from Figs. 3(b) and 3(d). This indicates the good quality of modeling the electron density of Mn and O. The deformation density is the difference between non-spherical multipole model and spherical independent atom model which can clearly reveal the valence electron distribution of bonding atoms. Figures 3(a) and 3(c) show the Mn–O_4 and Mn–O_2 plane in [MnO_6] octahedron. The overlap electrons between bonded Mn and O indicate the shared shell interaction, i.e., the covalent interaction of Mn–O bond. Quantum topological analysis of the total charge density can give the quantitative atomic interactions

based on the features of electrons at the bond critical points (BCPs), i.e., the maximum of electron density. According to the criterion in terms of the sign of $\nabla^2\rho\,(r_c)$, the Mn–O bond is shared covalent interaction, as the $\nabla^2\rho\,(r_c)$ between Mn and O is -0.7469, the negative Laplacian corresponding to the covalent bonding interaction.[18] However, the ratio of Hessian eigenvalues between the perpendicular and parallel directions in respect to the bond path $|\lambda_1/\lambda_3|$ is 0.6025 which is smaller than 1. This indicates that the covalency of Mn–O bond is relatively weak.[29] The covalency of the Mn–O bond is strongly correlated with Mn dissolution;[30] with increasing covalency of Mn–O bond, the dissolution of Mn can be reduced and the formation of John–Teller active Mn^{3+} can also be suppressed. In this work, the weak of covalency can be explained by the decrease of the oxygen content. Since the oxygen deficiency leads to the increasing amount of Mn^{3+}, with which the Mn–O bond is ionic. The decreasing covalent character of Mn–O interaction is strongly related to the capacity decay as shown in Fig. 1(f).

In summary, the electron accumulation between Mn and O atoms in deformation charge density map as well as the negative Laplacian and small $|\lambda_1/\lambda_3|$ at the BCP of Mn–O bond indicates a weak covalent interaction. This may relate with the oxygen deficiency of $LiMn_2O_4$ and correlate with the severe capacity fading from the initial charge/discharge process. A strategy on maintaining oxygen stoichiometry or increasing the valence state of Mn would be valid for preventing the Mn dissolution and capacity fading. As the x-ray electron density can be correlated with structure, future development of electron density on functional materials can be focused on the response on external field, i.e., temperature, strain, electric and magnetic fields, which can induce and control physical properties such as thermoelectricity, piezoelectricity, colossal magnetoresistance, etc. The ability to experimentally reveal the changes of electron redistribution and bonding interaction should have a great influence on the design of functional materials.

References

[1] Gu L, Xiao D D, Hu Y S, Li H and Ikuhara Y 2015 *Adv. Mater.* **27** 2134
[2] Choi J W and Aurbach D 2016 *Nat. Rev. Mater.* **1** 16013
[3] Wen Y, Xiao D, Liu X and Gu L 2017 *NPG Asia Mater.* **9** e360
[4] Ellis B L, Lee K T and Nazar L F 2010 *Chem. Mat.* **22** 691
[5] Park O K, Cho Y, Lee S, Yoo H C, Song H K and Cho J 2011 *Energy Environ. Sci.* **4** 1621
[6] Benedek R and Thackeray M M 2006 *Electrochem. Solid-State Lett.* **9** A265
[7] Deng B, Nakamura H and Yoshio M 2008 *J. Power Sources* **180** 864
[8] Li H, Luo Y, Xie J, Zhang Q and Yan L 2015 *J. Alloy. Compd.* **639** 346
[9] Manthiram A and Choi W 2007 *Electrochem. Solid-State Lett.* **10** A228
[10] Liu Q, Wang S, Tan H, Yang Z and Zeng J 2013 *Energies* **6** 1718
[11] Kim D K, Muralidharan P, Lee H W, Ruffo R, Yang Y, Chan C K, Peng H, Huggins R A and Cui Y 2008 *Nano Lett.* **8** 3948
[12] Stevens E D and Hope H 1977 *Acta Cryst.* **33** 723
[13] Streltsov V A, Belokoneva E L, Tsirelson V G and Hansen N K 1993 *Acta Cryst.* **49** 147
[14] Tolborg K and Iversen B B 2019 *Chem. Eur. J.* **25** 15010
[15] Toole N J O' and Streltsov V A 2001 *Phys. Rev. B* **57** 128
[16] Mondal S, Smaalen S van, Parakhonskiy G, Prathapa S J, Noohinejad L, Bykova E, Dubrovinskaia N, Chernyshov D and Dubrovinsky L 2013 *Phys. Rev. B* **88** 024118
[17] Scherer W, Hauf C, Presnitz M, Scheidt E W, Eickerling G, Eyert V, Hoffmann R D, Rodewald U C, Hammerschmidt A, Vogt C and Pöttgen R 2010 *Angew. Chem. Int. Edit.* **49** 1578
[18] Bader R F W and Essén H 1984 *J. Chem. Phys.* **80** 1943
[19] Bader R F W 1991 *Chem. Rev.* **91** 893
[20] Koritsanszky T S and Coppens P 2001 *Chem. Rev.* **101** 1583
[21] Kasai H, Tolborg K, Sist M, Zhang J, Hathwar V R, Filsø M Ø, Cenedese S, Sugimoto K, Overgaard J, Nishibori E and Iversen B B 2018 *Nat. Mater.* **17** 249
[22] Schmokel M S, Bjerg L, Larsen F K, Overgaard J, Cenedese S, Christensen M, Madsen G K H, Gatti C, Nishibori E, Sugimoto K, Takata M and Iversen B B 2013 *Acta Cryst.* **69** 570
[23] Wahlberg N, Bindzus N, Bjerg L, Becker J, Christensen S, Dippel A C, Jørgensen M R V and Iversen B B 2015 *J. Phys. Chem. C* **119** 6164
[24] Nishibori E, Sunaoshi E, Yoshida A, Aoyagi S, Kato K, Takata M and Sakata M 2007 *Acta Cryst.* **63** 43
[25] indzus N, Straaso T, Wahlberg N, Becker J, Bjerg L, Lock N, Dippel A C and Iversen B B 2014 *Acta Cryst.* **A70** 39
[26] Svane B, Tolborg K, Jørgensen L R, Roelsgaard M, Jorgensen M R V and Iversen B B 2019 *Acta Cryst.* **A75** 600
[27] Hunter J C 1981 *Journal of Solid State Chemistry* **39** 142
[28] Václav P, Michal D and Lukáš P 2014 *Z. Kristallogr.* **229** 345
[29] Gatti C 2005 *Z. Kristallogr.* **220** 399
[30] Kim Y, Lim J and Kang S 2013 *Int. J. Quantum Chem.* **113** 148